

Enhanced determination of emission fine structure and orientation of individual quantum dots based on correction algorithm for spectral diffusion

Pascal Gumbsheimer¹ , Frieder Conrad¹ , Yannic Behovits¹, Steffen Huber², Christopher Hinz¹, Carla Negele², Stefan Mecking² , Denis V Seletskiy^{1,3}  and Alfred Leitenstorfer¹ 

¹ Department of Physics and Center for Applied Photonics, University of Konstanz, Constance 78457, Germany

² Department of Chemistry, Chair of Chemical Materials Science, University of Konstanz, Constance 78464, Germany

E-mail: alfred.leitenstorfer@uni-konstanz.de

Received 4 November 2020, revised 17 December 2020

Accepted for publication 11 January 2021

Published 1 February 2021



CrossMark

Abstract

A robust algorithm based on cross-correlations and lucky imaging reliably allows the correction of spectrally diffused datasets. This step enables the resolution-limited analysis of the emission fine structure of semiconductor quantum dots (QDs). Bright and dark excitonic transitions are resolved with optimum signal-to-noise ratio, allowing for a precise determination of the angular direction of linear polarization of the different lines. The angular phases between polarization directions are intrinsically connected to the orientations of emission dipoles. This fact provides a tool for accurate numerical computation of the azimuth ϕ and polar angle θ of the QD with respect to the optical axis. Our *in-situ* characterization of QD fine structure and orientation represents a precise and non-invasive method without requiring specialized equipment beyond a standard luminescence setup. In this way, important information is provided whenever efficient coupling of a quantum emitter to the electromagnetic field is targeted by various nano- and micro-optic strategies.

Supplementary material for this article is available [online](#)

Keywords: semiconductor quantum dots, compound nanoparticles, spectral diffusion, optical properties, spatial orientation

(Some figures may appear in color only in the online journal)

³ Present address: Department of Engineering Physics, Polytechnique Montréal, Montréal H3T 1J4, Canada



Original content from this work may be used under the terms of the [Creative Commons Attribution 4.0 licence](#). Any further distribution of this work must maintain attribution to the author(s) and the title of the work, journal citation and DOI.

1. Introduction

Semiconductor quantum dots (QDs) are efficient emitters of single photons [1–4] and represent a promising resource for future quantum technologies [5]. In contrast to heralded single-photon generation based on spontaneous parametric downconversion [6, 7], they are able to provide a much higher and deterministic flux. Besides the powerful approaches based

on epitaxial QDs [8–10], high emission rates and remarkable photostability have also been demonstrated with core–shell nanoparticles [11–13]. However, spectral diffusion due to fluctuating electronic charges close to the surface of e.g. colloidal QDs are still hampering both precise analysis and applications of single-photon emission from such systems [14–18]. To handle this issue, we developed a cross-correlation-based algorithm exploiting the idea of lucky imaging [19] to efficiently correct for spectral diffusion. A typical photoluminescence (PL) setup is sufficient for the technique without a need for cumbersome extensions. As a first application of the correction, we present a method to determine the spatial orientation of the emission dipoles of a QD based on the polarization dependence of the fine structure. This information is important for optimizing light–matter coupling in nanophotonic systems. For example, it enables optimum embedding of the quantum system into an optical antenna or microresonator to minimize total internal reflection at the semiconductor–air interface and the divergence angle of emission [20–28]. Direct knowledge of the angular orientation of the crystallographic axes and spatial shape of such small nanoobjects can be obtained by imaging techniques offering atomic resolution as provided by e.g. high-resolution transmission electron microscopy (HRTEM) [29]. These axes and the shape determine the electronic confinement potential. Therefore, they are intrinsically linked to the directions of the transition dipoles which can be probed by exploiting the optical properties of the QD in e.g. polarization-sensitive measurements [30–35] or slight defocusing of images [36–41]. Still, the techniques to determine the 3D orientation often require a special sample preparation (HRTEM), non-standard equipment, cumbersome analysis and especially a precise understanding of the quantum system. For example, a slight deviation of state mixing or numerical aperture (NA) of the objective lens (OL) from nominal values result in a variation of angular modulation of the intensity in polarization-sensitive measurements or of the diffraction pattern in defocusing methods. In particular, the requirements are difficult to meet in a magnet cryostat where the OL is located inside the sample space. In this case, e.g. the NA might vary with the temperature of the OL. The accuracy of determining the orientation is limited also by the information about the eigenstates. This fact is especially true when analyzing uncharged QDs with a rich band-edge fine structure [17, 42, 43] and a time-dependent modulation of the degree of polarization [44]. The state mixing and the associated degree of polarization is mostly unknown and can only be pre-assigned assuming a defined shape of the confinement potential. These inaccuracies are caused by e.g. different elongation of the nanoparticle, crystallographic strain, or both. In total, existing methods for determining QD orientation are highly suitable for the unambiguous polarization profiles provided by e.g. quantum rods [31, 45, 46] or even more strongly elongated systems like nanobelts [47] in combination with a well-defined NA of the OL. Here, we present an *in-situ* method to optically determine the three-dimensional orientation of a QD only exploiting the relative polarization phases of different fine-structure lines, thus avoiding the uncertainties of other methods mentioned above and resulting in an enhanced

accuracy. To this end, a sufficient signal-to-noise ratio (SNR) of the fine structure of a single QD at high spectral resolution is required, as provided by our cross-correlation-based algorithm.

2. Sample system

First, we apply wet chemical synthesis to produce hybrid particles consisting of individual CdSe/CdS semiconductor nanocrystals embedded in a protective polymer nanoshell [48]. This approach provides a strong decoupling of the semiconductor from environmental influences, yielding emitters with improved blinking behavior of the PL emission and high photochemical stability, as well as discrete exciton–phonon coupling [49]. The ground state (GS) emission energy of the emitter can be tuned by adjusting the size of the CdSe core and the thickness of the CdS shell. The synthesis provides monocrystalline QDs with a hexagonal lattice structure [50]. QDs with an average CdSe core radius $R_{\text{CdSe}} = (2 \pm 0.4)$ nm and an average CdS shell radius $R_{\text{CdS}} = (4.5 \pm 0.6)$ nm exhibit a bright type-I semiconductor heterostructure at cryogenic temperatures [51]. The spatial dimensions of our system have been determined by TEM of the cores and the core–shell particles [28]. They are consistent with the energetic positions of excitonic emission [42, 52]. The particles exhibit relatively small deviations from rotational symmetry in the a – b plane perpendicular to the wurtzite c axis. The high repeatability in growth parameters features an emission peak of the ensemble centered at 635 nm with a narrow FWHM of 25 nm, reflecting the high homogeneity of the QDs [48]. In the hybrid particles, a single inorganic QD is encapsulated by a poly(methyl methacrylate) (PMMA) shell of a radius varying between 15 nm and 30 nm. The PMMA nanoshell improves both the photochemical as well as the mechanical stability, while also enabling persistent single-photon emission [48, 49]. For analysis, randomly oriented hybrid particles are spin-coated onto a (0001)-oriented quartz substrate at low density to allow for optical addressing of individual specimens.

It is now instructive to consider the fine structure of optical emission arising from recombination of the GS exciton X^0 to the global GS of the QD. X^0 is described by a total angular momentum $F = 2$. It is intrinsically split into four states with different angular momentum projections m_F . Adopting the notation $|F, m_F\rangle$, the bright exciton doublet is represented by $|2, \pm 1\rangle$. Radiative decay of the doublet $|2, \pm 2\rangle$ [42] to the GS is nominally dipole forbidden due to the overall change of m_F by ± 2 [17, 42, 53]. Electron–hole exchange (EHX) interactions lift the degeneracy of these states. Therefore, in QDs with a significant anisotropy in all three spatial directions, the pure $|2, \pm 1\rangle$ and $|2, \pm 2\rangle$ states are mixed, resulting in $|A_1\rangle = \frac{1}{\sqrt{2}}(|2, +1\rangle - |2, -1\rangle)$ and $|F_1\rangle = \frac{1}{\sqrt{2}}(|2, +2\rangle - |2, -2\rangle)$ which represent the initial states of interband transitions A_1 and F_1 to the GS. $|A_2\rangle$ and $|F_2\rangle$ are composed in an analogous way. The state mixing and assignment of the lines in the PL spectra discussed in section 4 is confirmed by the splitting behavior of the fine structure in

an external magnetic field (see supplementary material (available online at stacks.iop.org/JPD/54/155106/mmedia)). The moderate separation of the $|F_i\rangle$ states is dominated by the short-range EHX which results from the atomic crystal structure. In contrast, a larger energetic distance between the $|A_i\rangle$ states generally arises owing to the long-range EHX which also depends on the asymmetry of the electronic confinement potential. Typically, three discrete luminescence lines result from recombination to the GS, mostly including both A transitions and one F transition. At low temperatures, the other F transition is either degenerate due to a negligible short-range EHX or it suffers in intensity because of the combination of a weak dipole together with a low probability of occupation. The strong state-mixing process finally results in a linearly polarized emission for each of the components of the quadruplet [43, 54].

3. Experimental setup

The experiment for determining the orientation of the emission dipoles of a single QD including polarization-resolved spectroscopy at low temperatures is depicted in figure 1. We excite single QDs on a substrate using a femtosecond Er: fiber laser system operating at a repetition rate of 100 MHz [55] which provides a tuning range of the frequency-doubled output wavelength from 505 nm to 650 nm [56]. The sample is located in a stabilized magnet cryostat offering variable sample temperatures between 3.5 K and 300 K. The measurement is performed in reflection geometry and allows targeted excitation of single QDs. They are deposited on a (0001)-oriented quartz substrate using a spin-coating process, resulting in an average distance of single particles of $(2.4 \pm 0.8) \mu\text{m}$. The sample holder is mounted with three stick-slip motors with a full driving range of at least 5 mm in each direction (x , y , z). The sub-nm fine positioning resolution allows addressing of a single nanoparticle. The QD emission is collected via a cryogenic OL ($\text{NA} = 0.82$) and separated from the excitation light using a dichroic beam splitter and an additional long-pass filter. The luminescence is resolved both in polarization and energy using a combination of a half-wave plate and a Glan–Thompson polarizer in front of a grating monochromator. Finally, an electron-multiplying CCD (EMCCD) camera offers single-photon sensitivity.

4. Luminescence experiments and correction algorithm

To explore the considerations from section 2, single QDs at a sample temperature of 6 K are addressed by our laser system tuned to the quasicontinuum of densely packed absorption lines approximately 100 meV above X^0 (see figure 2(a)). The hot exciton decays into X^0 by phonon-assisted relaxation with rate γ and recombines to the GS. The polarization of the emission is determined by a Glan–Thompson polarizer with an extinction ratio of 10^{-6} and an achromatic half-wave plate, defining a polar angle α between the principal axes of both components (see figure 2(b)).

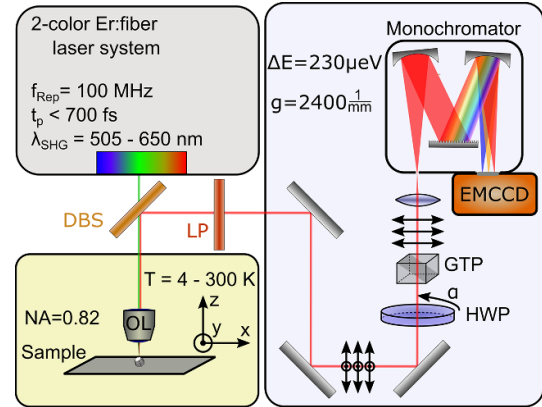


Figure 1. Experimental setup and detection scheme. A widely tunable Er: fiber laser system provides a frequency-doubled wavelength range of $\lambda_{\text{SHG}} = (505\text{--}650)$ nm with variable pulse duration in the femto- and sub-picosecond range. An objective lens ($\text{NA} = 0.82$) allows to study the emission properties of individual QDs. For the alignment, piezo-based stick-slip motors offer a sub-nm resolution of positioning of the sample in x , y and z direction. With a dichroic beam splitter (DBS) and an additional long-pass filter (LP), the nanocrystal photoluminescence signal is separated from the excitation light. The polarization states of the incident photons are modified using a half-wave plate (HWP) and projected in the detection [57] plane with a Glan–Thompson polarizer (GTP). The QD emission is analyzed in a grating monochromator with a spectral resolution of $230 \mu\text{eV}$ and an electron-multiplying CCD camera (EMCCD).

A time series of 100 PL emission spectra of a single CdSe/CdS/PMMA hybrid particle (QD I) with an individual integration time of 1 s is depicted in the upper panel of figure 3(a). Here, the polarization angle is set to $\alpha = 70^\circ$.

The emission is characterized by discrete shifts in the energetic position which are likely caused by charge fluctuations in the microscopic environment [18]. Owing to the protective PMMA shell, the jumps occur on a typical time scale significantly longer than the integration period required for a highly resolved spectrum with an SNR adequate for detecting individual fine-structure lines. When aiming for further improvement of the SNR, the direct sum $\text{PL}_{\alpha=70^\circ}$ over all spectra results in a vanishing contrast of the emission fine structure (lower panel in figure 3(a)).

To circumvent this issue, we have developed a fully automated post-processing correction of the spectral diffusion based on a cross-correlation algorithm exploiting the idea of lucky imaging [19]. The similarity of two spectra $I_i(E)$ and $I_j(E)$ including an energetic shift Δ is judged by the cross-correlation coefficient

$$C_{i,j}(\Delta) := [I_i * I_j](\Delta) = \sum_{E=E_{\min}}^{E_{\max}} I_i(E) I_j(E + \Delta), \quad (1)$$

where E_{\min} and E_{\max} define the spectral boundaries. The cross-correlation function $C_{i,j}(\Delta)$ is evaluated for all relative energetic shifts Δ between both spectra with $E_{\min} - E_0 \leq \Delta \leq E_{\max} - E_0$. E_0 is the energetic position of the maximal amplitude in I_j . The maximum of $C_{i,j}(\Delta)$ determines the energy shift Δ

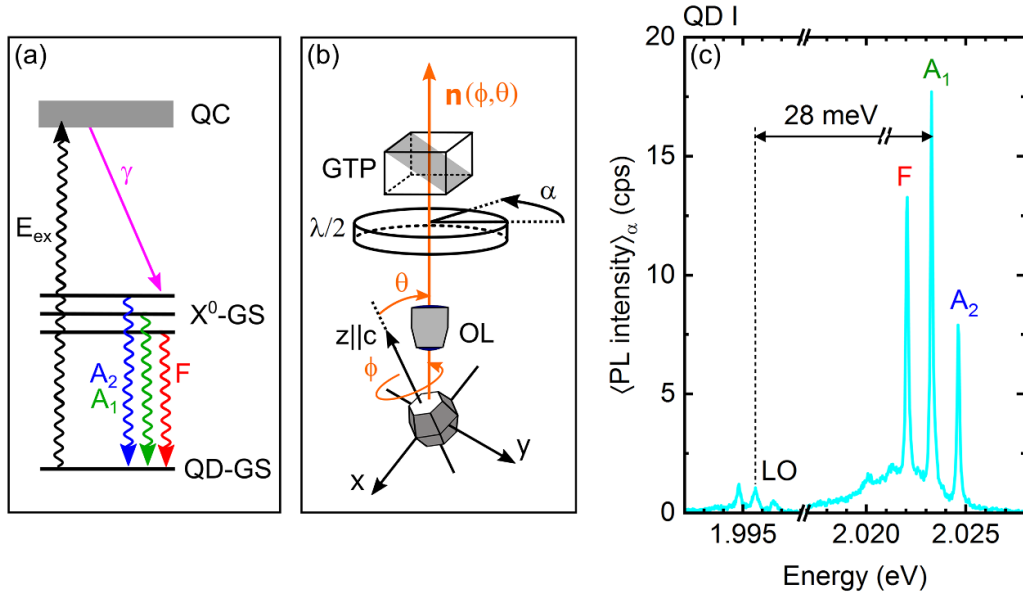


Figure 2. Energetic level structure, measurement principle and PL of a single nanocrystal at a cryogenic temperature of $T = 6$ K. (a) Excitation of the QD ($E_{ex} = 2.168$ eV) to the quasicontinuum (QC) is followed by rapid non-radiative relaxation γ to the exciton ground states (X^0 -GS) and a radiative recombination to the QD ground state (QD-GS) resulting in three fine-structure lines A_1 , A_2 and F . (b) The random orientation of the QD on the substrate with respect to the direction of observation $\mathbf{n}(\phi, \theta)$ is described by the azimuth ϕ and polar angle θ . The QD PL signal is detected by an objective lens (OL) with NA = 0.82 at various polarization angles α selected with a half-wave plate ($\lambda/2$) and a Glan–Thompson polarizer (GTP). (c) Spectrally resolved PL signal $\langle \text{PL intensity} \rangle_\alpha$ of a single CdSe/CdS/PMMA hybrid particle, as averaged over all polarization angles.

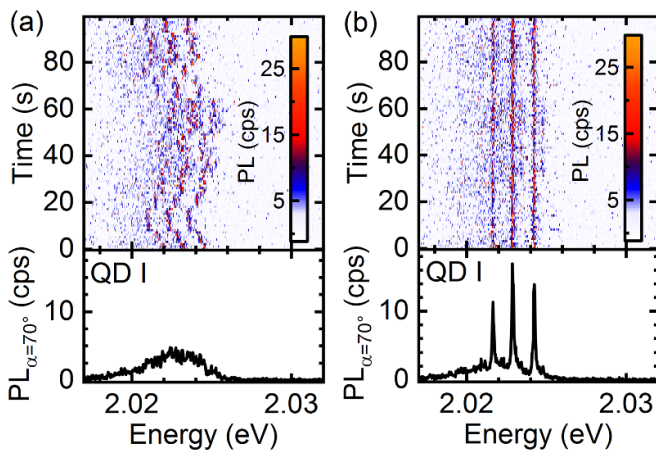


Figure 3. Comparison of the uncorrected and corrected PL emission from QD I for a polarization angle of $\alpha = 70^\circ$. (a) Time series of 100 color coded PL spectra with an individual exposure time of 1 s (upper panel). Due to spectral diffusion, the emission fine structure is lost when integrating over all spectra (lower panel). (b) Result of the standardized algorithm for removing the spectral jitter of the data depicted in (a) (upper panel). Averaging over the corrected spectra results in a data set with enhanced signal-to-noise ratio and a fine structure limited by the resolution of the monochromator (lower panel).

yielding the best overlap between the two spectra. For each individual spectrum $I_k(E)$, we can now compute a characteristic quantity D_k which serves as a measure

for the similarity of this spectrum with all other spectra $I_n(E)$:

$$D_k := \sum_{n \neq k} \max(C_{k,n}(\Delta)). \quad (2)$$

In the spirit of lucky imaging, the reference spectrum exhibiting the highest structural similarity with respect to all other spectra is characterized by the maximum global value of D_k . This reference spectrum is now exploited to determine the spectral shift Δ_j of all remaining spectra by searching for the maximum in $C_{k,j}$. We can now set a threshold in the absolute value of $C_{k,j}(\Delta_j)$ to discard the spectra with insufficient information content. Such data sets emerge e.g. when a spectral jump occurs during a specific integration interval. All remaining spectra $I_j(E)$ are subsequently shifted in energy by Δ_j and summed up. This step results in a data set which conserves the energetic fine structure at a drastically improved SNR. The results of this procedure applied to the data from the upper part of figure 3(a) are depicted in the upper part of figure 3(b). Finally, the averaged sum is shown in the lower part of figure 3(b). Very interestingly, this step results in a spectral width of individual fine-structure lines of approximately $270 \mu\text{eV}$ which is close to the nominal energy resolution of our spectrometer of $230 \mu\text{eV}$. This finding clearly demonstrates a high efficiency and reliability of our correction algorithm (see supplementary material for a quantitative analysis). Obviously, the spectral diffusion results only in a small perturbation to the excitonic quantum confinement and

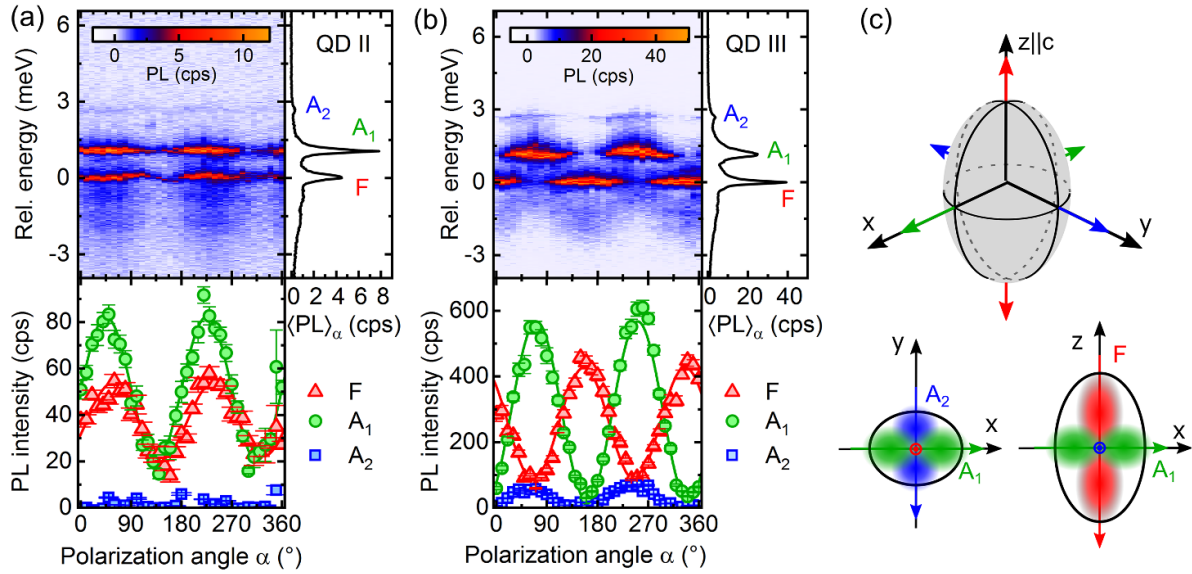


Figure 4. Polarization properties of emission fine structure and schematic of effective dipole orientations of an asymmetric QD. Top parts of (a) and (b), left: PL intensity color coded as a function of polarization angle and relative photon energy of two randomly oriented QDs II and III at a temperature of $T = 6$ K. The polarization-averaged signals $\langle \text{PL} \rangle_\alpha$ are depicted at right, respectively. Bottom parts of (a) and (b): spectral slices around emission maxima F (red triangles), A_1 (green dots) and A_2 (blue squares) as a function of polarization angle. The full lines represent least-square fits based on equation (3). (c) Schematic of dipolar emission from a QD with wurtzite crystal structure. The crystallographic c axis is oriented along z and a slight distortion of the confinement potential exists in the x - y plane. Effective dipole axes related to transitions F , A_1 and A_2 are indicated by red, green and blue arrows on top, respectively, and projections of the corresponding dipolar emission patterns onto the x - y and y - z planes are depicted at the bottom following the same color coding. Here, the left scheme represents the direction of view onto QD II and QD III is oriented close to the situation at right.

changes mainly the total bandgap energy of the QD. Therefore, the exciton fine structure is hardly affected.

5. Analysis of three-dimensional orientation

As a first example, we depict fine-structure PL of the single CdSe/CdS/PMMA nanoparticle QD I (figure 2(c)). The measurement of the PL is averaged over the polarization angles α $\langle \text{PL} \rangle_\alpha$. It reveals three fine-structure lines labeled F , A_1 and A_2 . In this QD, the F transition is two-fold degenerate containing both projections $m_F = \pm 2$ of the total angular momentum of the exciton. The weak pedestal with discrete resonances appearing approximately 1 meV and 2 meV below the zero-phonon lines originates from the emission of photons together with acoustic phonons [49, 58]. Owing to the improved SNR, all fine-structure lines are clearly resolved also in the excitonic recombination assisted by emission of a longitudinal-optical phonon which is red shifted by 28 meV [53].

To illustrate the physical principles for determining the orientation, the luminescence of two other QDs (II and III) with high-symmetry configurations is studied in figure 4. The total emission intensity of both QDs is depicted as a function of energy relative to the F line in the right panel of figures 4(a) and (b), respectively. As in figure 2(c), all three fine-structure lines are resolved. The luminescence emission spectra are color coded as a function of polarization angle α in the left panels. The stability of our QDs in combination with a relatively fast scan over all polarization angles leads to a robust periodic modulation with pronounced differences

in the relative phase between the lines for QD II and QD III. To investigate the origin of this variation, we now perform a quantitative analysis with a spectral integration over the intensity of each line. The results are depicted in the lower panels of figures 4(a) and (b), respectively. The full lines represent least-square fits to the data based on the angular intensity characteristics expected for a dipole-like emission of each line [32]:

$$I(\alpha) = I_m \cos^2(\alpha - \phi_0) + I_0. \quad (3)$$

Here I_m and I_0 represent the modulation amplitude and amplitude offset, respectively, and ϕ_0 is a phase offset. We define the degree of linear polarization to be

$$p = \frac{I_m}{I_m + I_0}. \quad (4)$$

Regarding equation (4), we find an average degree of linear polarization of $p = 0.81 \pm 0.16$ for all lines. The deviation from perfect linear polarization with $p = 1$ is caused predominantly by the detection through a high-NA objective [32]. In the selected examples of figure 4, the polarization of the F and A_1 lines reveals an in-phase behavior for QD II and an out-of-phase behavior for QD III, respectively. As discussed below, this difference is caused by the three-dimensional orientation of each QD with respect to the optical axis, resulting in an angle-dependent projection of the emitting dipoles.

We first introduce a unit vector $\mathbf{n}(\phi, \theta)$ as a function of the azimuth angle ϕ and polar angle θ defining the observation

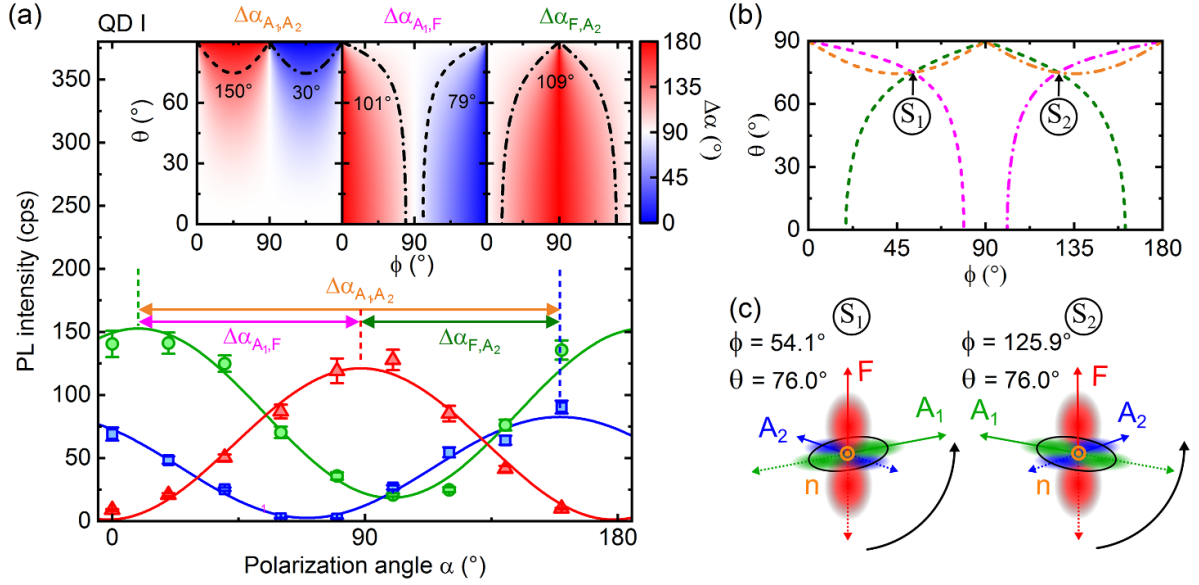


Figure 5. Extraction of the orientation of QD I with respect to the optical axis \mathbf{n} . (a) Spectrally integrated PL intensity of all three fine-structure lines F (red triangles), A_1 (green dots) and A_2 (blue squares) versus polarization angle α . Least-square sinusoidal fits (full lines) based on equation (3) lead to relative phase differences of $\Delta\alpha_{A_1,F} = 79.2^\circ \pm 2.5^\circ$, $\Delta\alpha_{F,A_2} = 70.9^\circ \pm 2.6^\circ$ and $\Delta\alpha_{A_1,A_2} = 150.2^\circ \pm 2.8^\circ$, respectively. Insets: relative phase differences calculated with equation (7) and its equivalents color coded as a function of angles ϕ and θ . Dashed contour lines belong to the measured values of angles $\Delta\alpha_i$ and dash-dotted lines indicate values of $180^\circ - \Delta\alpha_i$, respectively. (b) The three contour lines defined in (a) for all $\Delta\alpha_i$ versus angles ϕ and θ . The intersection points S_1 and S_2 are defining two possible angular orientations of the QD in (ϕ, θ) space. (c) Projections of the associated dipoles, oscillating directions (colored arrows) and sketch of the confinement potential in the x - y plane (black ellipses) for the two configurations S_1 and S_2 . The relative order of intensity maxima following the black arrows is different for both orientations. In our example, the order of $A_1 \rightarrow F \rightarrow A_2$ of maxima depicted in (a) assigns the correct orientation of QD I to S_1 , resulting in $\phi = 54.1^\circ \pm 6.2^\circ$ and $\theta = 76.0^\circ \pm 2.1^\circ$.

direction with respect to the crystallographic c axis of the wurtzite-type hexagonal lattice of each QD (see figure 2(b)):

$$\mathbf{n}(\phi, \theta) = \begin{pmatrix} \sin(\theta) \cos(\phi) \\ \sin(\theta) \sin(\phi) \\ \cos(\theta) \end{pmatrix}. \quad (5)$$

In these coordinates, the z direction coincides with the c axis while the x and y directions accord with the shorter and longer main axes of the elliptical confinement potential of the QD in the a - b plane, respectively (see figure 4(c)). The probability of different GS transitions strongly depends on the polarization angle of the emitted light. The F transitions are preferentially polarized along the c axis [59, 60]. In contrast, the transition matrix element P_{GS}^A related to the bright A transitions exhibits a maximum if the polarization vector \mathbf{e} of the emitted light is perpendicular to the c axis [42]:

$$P_{\text{GS}}^A = |\langle \text{GS} | \mathbf{e} \hat{\mathbf{p}} | \mathbf{n} \rangle| \propto \sin^2(\theta), \quad (6)$$

where $\hat{\mathbf{p}}$ is the momentum operator. In case of a lifted degeneracy of the $|A\rangle$ states resulting in $|A_1\rangle$ and $|A_2\rangle$, the two dipole axes are perpendicular to each other [43] and they are aligned parallel to the short and long axis of the confinement potential. As defined in figure 4(c), the effective dipoles \mathbf{e}_{A_1} , \mathbf{e}_{A_2} and \mathbf{e}_F are oriented along \mathbf{e}_x , \mathbf{e}_y and \mathbf{e}_z , respectively. The examples in figures 4(a) and (b) have been selected because they may be understood intuitively: the in-phase behavior of the F and A_1 emission in figure 4(a) directly indicates that the \mathbf{e}_x - \mathbf{e}_z plane

of QD II includes the direction of observation and therefore, $\phi \approx 0^\circ$. From the out-of-phase behavior of the F transition with respect to both A transitions of QD III (figure 4(b)), \mathbf{n} has to be parallel to the \mathbf{e}_x - \mathbf{e}_y plane with $\theta \approx 90^\circ$.

For the vast majority of randomly oriented QDs, such a straightforward determination of both polarization angles is impossible. The polarization-resolved PL intensity of a QD with arbitrary orientation (QD I) is depicted in figure 5(a). Here, the full information is encoded in the relative phase differences $\Delta\alpha_{A_1,F}$, $\Delta\alpha_{F,A_2}$ and $\Delta\alpha_{A_1,A_2}$ between all pairs of fine-structure transitions. We perform least-square fits to the angle-dependent PL intensity according to equation (3) and calculate the difference in phase offsets like e.g. $\Delta\alpha_{A_1,F} = \phi_{0,F} - \phi_{0,A_1}$. In this way, we find $\Delta\alpha_{A_1,F} = 79.2^\circ \pm 2.5^\circ$, $\Delta\alpha_{F,A_2} = 70.9^\circ \pm 2.6^\circ$ and $\Delta\alpha_{A_1,A_2} = 150.2^\circ \pm 2.8^\circ$. It is now important to remember that the polarization of the luminescence is determined by the projection \mathbf{e}' of the emitting dipole \mathbf{e} with respect to the plane perpendicular to the detection axis $\mathbf{n}(\phi, \theta)$. For the two dipole projections \mathbf{e}'_{A_1} and \mathbf{e}'_{A_2} , corresponding to the transitions A_1 and A_2 , this fact leads to an angle difference

$$\begin{aligned} \Delta\alpha_{A_1,A_2} &= \arccos\left(\frac{\mathbf{e}'_{A_1} \cdot \mathbf{e}'_{A_2}}{|\mathbf{e}'_{A_1}| |\mathbf{e}'_{A_2}|}\right) \\ &= \arccos\left(\frac{-\sin^2(\theta) \cos(\phi) \sin(\phi)}{|\mathbf{e}'_{A_1}(\theta, \phi)| |\mathbf{e}'_{A_2}(\theta, \phi)|}\right). \end{aligned} \quad (7)$$

Our strategy to extract the angles θ and ϕ from equation (7) and its equivalents for the other two pairs of transitions is as follows: calculating $\Delta\alpha_{A_1, A_2}$ for all combinations of θ and ϕ leads to the two-dimensional relation between in the left upper inset of figure 5(a). For QD I where $\Delta\alpha_{A_1, A_2} = 150^\circ$ and $180^\circ - \Delta\alpha_{A_1, A_2} = 30^\circ$, the dashed and dash-dotted lines result connecting pairs of values of ϕ and θ which are compatible with this measurement. The relationships for $\Delta\alpha_{A_1, F}(\phi, \theta)$ and $\Delta\alpha_{F, A_2}(\phi, \theta)$ are color coded in the center and right insets of figure 5(a). Again, all pairs of values for ϕ and θ compatible with the measured difference angles are indicated by the dashed and dash-dotted lines. All relations must be fulfilled simultaneously, resulting in two intersection points S_1 and S_2 in figure 5(b) where all contour lines determined in the insets of figure 5(a) have been plotted together. From this analysis, we find $\theta = 76.0^\circ$ and either $\phi = 54.1^\circ$ or $\phi = 125.9^\circ$ for QD I. In order to resolve the remaining ambiguity, the absolute polarization phases ϕ_0 of all fine-structure lines, as defined by equation (3), and the associated order of intensity maxima have to be taken into account. From the sketch in figure 5(c), it follows that the sequence of the intensity maxima according to $\dots \rightarrow A_1 \rightarrow F \rightarrow A_2 \rightarrow A_1 \rightarrow \dots$ belongs to $\phi = 54.1^\circ$ and a permuted ordering to $\phi = 125.9^\circ$, respectively. In our case, we observe an order following case S_1 , finally assigning an orientation of $\phi = 54.1^\circ \pm 6.2^\circ$ and $\theta = 76.0^\circ \pm 2.1^\circ$ to QD I. The high precision of our method is evident from the small error margins which are calculated according to the supplementary material.

6. Summary and outlook

In conclusion, a robust algorithm based on the idea of lucky imaging is exploited to eliminate spectral fluctuations of the luminescence fine structure of individual nanosystems. Our method is not only limited to QD emission spectra at cryogenic temperatures, but also applicable whenever spectral jitter limits long-term integration of PL measurements. As a first application enabled by this tool, an all-optical way to determine the three-dimensional orientation of emission dipoles of individual quantum emitters with respect to the axis of observation is demonstrated. The angular position is provided with an accuracy of a few degrees by this fast and reliable approach. Further improvement may be easily implemented exploiting options to cancel out intensity fluctuations of a QD offered, e.g. by parallel detection of different polarization components [43] or enhanced total integration times in combination with fast variation of the polarization angle. Our correction method is of great benefit whenever a maximally precise determination of emission patterns is important that are subject to temporal shifts. For example, the capability to identify the spatial orientation of an emitter with standard equipment present in typical luminescence setups is helpful to assemble compound nanosystems providing a maximum of light-matter coupling. These implementations are also of great importance whenever anisotropic physical properties of nanoobjects are to be determined like e.g. the angle-dependent g factors of quantum-confined electrons in a magnetic field [61–63].

Acknowledgment

This work was funded by the DFG through Collaborative Research Center SFB 767. D. V. Seletskiy acknowledges support from a Marie Curie Fellowship by the Zukunftscolleg at University of Konstanz, the Baden-Württemberg Stiftung, and DFG Grant #SE 2443/2-1. The authors declare no competing financial interest.

ORCID iDs

Pascal Gumbsheimer  <https://orcid.org/0000-0001-5563-6207>

Frieder Conradt  <https://orcid.org/0000-0003-4239-9956>

Stefan Mecking  <https://orcid.org/0000-0002-6618-6659>

Denis V Seletskiy  <https://orcid.org/0000-0003-3480-4595>

Alfred Leitenstorfer  <https://orcid.org/0000-0002-9847-257X>

References

- [1] Michler P, Kiraz A, Becher C, Schoenfeld W V, Petroff P M, Zhang L, Hu E and Imamoglu A 2000 A quantum dot single-photon turnstile device *Science* **290** 2282–5
- [2] Santori C, Pelton M, Solomon G, Dale Y and Yamamoto Y 2001 Triggered single photons from a quantum dot *Phys. Rev. Lett.* **86** 186
- [3] Zwiller V, Blom H, Jonsson P, Panev N, Jeppesen S, Tsegaye T, Goobar E, Pistol M E, Samuelson L and Björk G 2001 Single quantum dots emit single photons at a time: antibunching experiments *Appl. Phys. Lett.* **78** 2476–8
- [4] Yuan Z, Kardynal B E, Stevenson R M, Shields A J, Lobo C J, Cooper K, Beattie N S, Pepper M and Pepper M 2002 Electrically driven single-photon source *Science* **295** 102–5
- [5] Somaschi N *et al* 2016 Near-optimal single-photon sources in the solid state *Nat. Photon.* **10** 340–5
- [6] Guo X, Zou C L, Schuck C, Jung H, Cheng R and Tang H X 2017 Parametric down-conversion photon-pair source on a nanophotonic chip *Light Sci. Appl.* **6** e16249
- [7] Zhang H *et al* 2011 Preparation and storage of frequency-uncorrelated entangled photons from cavity-enhanced spontaneous parametric downconversion *Nat. Photon.* **5** 628–32
- [8] Yoshie T, Scherer A, Hendrickson J, Khitrova G, Gibbs H M, Rupper G, Ell C, Shchekin O B and Deppe D G 2004 Vacuum Rabi splitting with a single quantum dot in a photonic crystal nanocavity *Nature* **432** 200–3
- [9] Reithmaier J P, Sek G, Löffler A, Hofmann C, Kuhn S, Reitzenstein S, Keldysh L V, Kulakovskii V D, Reinecke T L and Forchel A 2004 Strong coupling in a single quantum dot-semiconductor microcavity system *Nature* **432** 197–200
- [10] Peter E, Senellart P, Martrou D, Lemaître A, Hours J, Gérard J M and Bloch J 2005 Exciton–photon strong-coupling regime for a single quantum dot embedded in a microcavity *Phys. Rev. Lett.* **95** 067401
- [11] Dabbousi B O, Rodriguez-Viejo J, Mikulec F V, Heine J R, Mattoussi H, Ober R, Jensen K F and Bawendi M G 1997 (CdSe)ZnS core–shell quantum dots: synthesis and characterization of a size series of highly luminescent nanocrystallites *J. Phys. Chem. B* **101** 9463–75
- [12] Reiss P, Bleuse J and Pron A 2002 Highly luminescent CdSe/ZnSe core/shell nanocrystals of low size dispersion *Nano Lett.* **2** 781–4

- [13] Peng X, Schlamp M C, Kadavanich A V and Alivisatos A P 1997 Epitaxial growth of highly luminescent CdSe/CdS core/shell nanocrystals with photostability and electronic accessibility *J. Am. Chem. Soc.* **119** 7019–29
- [14] Empedocles S A and Bawendi M G 1997 Quantum-confined stark effect in single CdSe nanocrystallite quantum dots *Science* **278** 2114–7
- [15] Empedocles S A and Bawendi M G 1999 Influence of spectral diffusion on the line shapes of single CdSe nanocrystallite quantum dots *J. Phys. Chem. B* **103** 1826–30
- [16] Gómez D E, van Embden J and Mulvaney P 2006 Spectral diffusion of single semiconductor nanocrystals: the influence of the dielectric environment *Appl. Phys. Lett.* **88** 154106
- [17] Biadala L, Louyer Y, Tamarat P and Lounis B 2009 Direct observation of the two lowest exciton zero-phonon lines in single CdSe/ZnS nanocrystals *Phys. Rev. Lett.* **103** 037404
- [18] Beyler A P, Marshall L F, Cui J, Brokmann X and Bawendi M G 2013 Direct observation of rapid discrete spectral dynamics in single colloidal CdSe–CdS core–shell quantum dots *Phys. Rev. Lett.* **111** 177401
- [19] Law N M, Mackay C D and Baldwin J E 2006 Lucky imaging: high angular resolution imaging in the visible from the ground *Astron. Astrophys.* **446** 739–45
- [20] Fan X, Palinginis P, Lacey S, Wang H and Lonergan M C 2000 Coupling semiconductor nanocrystals to a fused-silica microsphere: a quantum-dot microcavity with extremely high Q factors *Opt. Lett.* **25** 1600–2
- [21] Farahani J N, Pohl D W, Eisler H J and Hecht B 2005 Single quantum dot coupled to a scanning optical antenna: a tunable superemitter *Phys. Rev. Lett.* **95** 017402
- [22] Wu Z, Mi Z, Bhattacharya P, Zhu T and Xu J 2007 Enhanced spontaneous emission at 1.55 μm from colloidal PbSe quantum dots in a Si photonic crystal microcavity *Appl. Phys. Lett.* **90** 171105
- [23] Kahl M *et al* 2007 Colloidal quantum dots in all-dielectric high-Q pillar microcavities *Nano Lett.* **7** 2897–900
- [24] Pfeiffer M, Lindfors K, Atkinson P, Rastelli A, Schmidt O G, Giessen H and Lippitz M 2012 Positioning plasmonic nanostructures on single quantum emitters *Phys. Status Solidi* **249** 678–86
- [25] de Geyter B, Komorowska K, Brainis E, Emplit P, Geiregat P, Hassinen A, Hens Z and van Thourhout D 2012 From fabrication to mode mapping in silicon nitride microdisks with embedded colloidal quantum dots *Appl. Phys. Lett.* **101** 161101
- [26] Ureña E B, Kreuzer M P, Itzhakov S, Rigneault H, Quidant R, Oron D and Wenger J 2012 Excitation enhancement of a quantum dot coupled to a plasmonic antenna *Adv. Mater.* **24** OP314–20
- [27] Regler A, Schraml K, Lyamkina A A, Spiegel M, Müller K, Vuckovic J, Finley J J and Kaniber M 2016 Emission redistribution from a quantum dot-bowtie nanoantenna *J. Nanophotonics* **10** 033509
- [28] Werschler F *et al* 2018 Efficient emission enhancement of single CdSe/CdS/PMMA quantum dots through controlled near-field coupling to plasmonic bullseye resonators *Nano Lett.* **18** 5396–400
- [29] Lee H S, Lee J Y, Kim T W and Kim M D 2003 Strain effects in and crystal structures of self-assembled InAs/GaAs quantum dots *Appl. Phys. Lett.* **83** 2256–8
- [30] Empedocles S A, Neuhauser R and Bawendi M G 1999 Three-dimensional orientation measurements of symmetric single chromophores using polarization microscopy *Nature* **399** 126–30
- [31] Ohmachi V M, Komori Y, Iwane A H, Fujii F, Jin T and Yanagida T 2012 Fluorescence microscopy for simultaneous observation of 3D orientation and movement and its application to quantum rod-tagged myosin V *Proc. Natl Acad. Sci. USA* **109** 5294–8
- [32] Lethiec C, Laverdant J, Vallon H, Javaux C, Dubertret B, Frigerio J M, Schwob C, Coolen L and Maître A 2014 Measurement of three-dimensional dipole orientation of a single fluorescent nanoemitter by emission polarization analysis *Phys. Rev. X* **4** 021037
- [33] Vezzoli S, Manceau M, Leménager G, Glorieux Q, Giacobino E, Carbone L, de Vittorio M and Bramati A 2015 Exciton fine structure of CdSe/CdS nanocrystals determined by polarization microscopy at room temperature *ACS Nano* **9** 7992–8003
- [34] Feng F, Nguyen L T, Nasilowski M, Nadal B, Dubertret B, Maître A and Coolen L 2018 Probing the fluorescence dipoles of single cubic CdSe/CdS nanoplatelets with vertical or horizontal orientations *ACS Photonics* **5** 1994–9
- [35] Becker M A *et al* 2018 Bright triplet excitons in caesium lead halide perovskites *Nature* **553** 189–93
- [36] Jasny J and Sepiøl J 1997 Single molecules observed by immersion mirror objective. A novel method of finding the orientation of a radiating dipole *Chem. Phys. Lett.* **273** 439–43
- [37] Lieb M A, Zavislan J M and Novotny L 2004 Single-molecule orientations determined by direct emission pattern imaging *J. Opt. Soc. Am. B* **21** 1210
- [38] Patra D, Gregor I and Enderlein J 2004 Image analysis of defocused single-molecule images for three-dimensional molecule orientation studies *J. Phys. Chem. A* **108** 6836–41
- [39] Patra D, Gregor I, Enderlein J and Sauer M 2005 Defocused imaging of quantum-dot angular distribution of radiation *Appl. Phys. Lett.* **87** 101103
- [40] Schuster R, Barth M, Gruber A and Cichos F 2005 Defocused wide field fluorescence imaging of single CdSe/ZnS quantum dots *Chem. Phys. Lett.* **413** 280–3
- [41] Brokmann X, Ehrensperger M V, Hermier J P, Triller A and Dahan M 2005 Orientational imaging and tracking of single CdSe nanocrystals by defocused microscopy *Chem. Phys. Lett.* **406** 210–4
- [42] Efros A L, Rosen M, Kuno M, Nirmal M, Norris D and Bawendi M 1996 Band-edge exciton in quantum dots of semiconductors with a degenerate valence band: dark and bright exciton states *Phys. Rev. B* **54** 4843–56
- [43] Htoon H, Furis M, Crooker S A, Jeong S and Klimov V I 2008 Linearly polarized ‘fine structure’ of the bright exciton state in individual CdSe nanocrystal quantum dots *Phys. Rev. B* **77** 35328
- [44] Montiel D and Yang H 2008 Observation of correlated emission intensity and polarization fluctuations in single CdSe/ZnS quantum dots *J. Phys. Chem. A* **112** 9352–5
- [45] Hu J, Li L S, Yang W, Manna L, Wang L W and Alivisatos A P 2001 Linearly polarized emission from colloidal semiconductor quantum rods *Science* **292** 2060–3
- [46] Chen X, Nazzal A, Goorskey D, Xiao M, Peng Z A and Peng X 2001 Polarization spectroscopy of single CdSe quantum rods *Phys. Rev. B* **64** 245304
- [47] Datar A, Balakrishnan K, Yang X, Zuo X, Huang J, Oitker R, Yen M, Zhao J, Tiede D M and Zang L 2006 Linearly polarized emission of an organic semiconductor nanobelt *J. Phys. Chem. B* **110** 12327–32
- [48] Negele C, Haase J, Budweg A, Leitenstorfer A and Mecking S 2013 Stable single-photon emission by quantum dot/polymer hybrid particles *Macromol. Rapid Commun.* **34** 1145–50
- [49] Werschler F, Hinz C, Froning F, Gumbsheimer P, Haase J, Negele C, de Roo T, Mecking S, Leitenstorfer A and Seletskiy D V 2016 Coupling of excitons and discrete acoustic phonons in vibrationally isolated quantum emitters *Nano Lett.* **16** 5861–5

- [50] Mahler B, Spinicelli P, Buil S, Quelin X, Hermier J P and Dubertret B 2008 Towards non-blinking colloidal quantum dots *Nat. Mater.* **7** 659–64
- [51] Reiss P, Protière M and Li L 2009 Core/shell semiconductor nanocrystals *Small* **5** 154–68
- [52] Chen Y, Vela J, Htoon H, Casson J L, Werder D J, Bussian D A, Klimov V I and Hollingsworth J A 2008 Giant multishell CdSe nanocrystal quantum dots with suppressed blinking *J. Am. Chem. Soc.* **130** 5026–7
- [53] Louyer Y, Biadala L, Tamarat P and Lounis B 2010 Spectroscopy of neutral and charged exciton states in single CdSe/ZnS nanocrystals *Appl. Phys. Lett.* **96** 203111
- [54] Bayer M *et al* 2002 Fine structure of neutral and charged excitons in self-assembled In(Ga)As/(Al) GaAs quantum dots *Phys. Rev. B* **65** 195315
- [55] Sotier F, Thomay T, Hanke T, Korger J, Mahapatra S, Frey A, Brunner K, Bratschitsch R and Leitenstorfer A 2009 Femtosecond few-fermion dynamics and deterministic single-photon gain in a quantum dot *Nat. Phys.* **5** 352–6
- [56] Hinz C *et al* 2018 Charge and spin control of ultrafast electron and hole dynamics in single CdSe/ZnSe quantum dots *Phys. Rev. B* **97** 045302
- [57] Bigot L, Jurdyc A, Jacquier B, Gasca L and Bayart D 2002 Resonant fluorescence line narrowing measurements in erbium-doped glasses for optical amplifiers *Phys. Rev. B* **66** 214204
- [58] Kosako T, Kadoya Y and Hofmann H F 2010 Directional control of light by a nano-optical Yagi–Uda antenna *Nat. Photon.* **4** 312–5
- [59] Bawendi M G, Carroll P J, Wilson W L and Brus L E 1992 Luminescence properties of CdSe quantum crystallites: resonance between interior and surface localized states *J. Chem. Phys.* **96** 946–54
- [60] Califano M, Franceschetti A and Zunger A 2007 Lifetime and polarization of the radiative decay of excitons, biexcitons, and trions in CdSe nanocrystal quantum dots *Phys. Rev. B* **75** 115401
- [61] Witek B J, Heeres R W, Perinetti U, Bakkens E P A M, Kouwenhoven L P and Zwiller V 2011 Measurement of the g-factor tensor in a quantum dot and disentanglement of exciton spins *Phys. Rev. B* **84** 195305
- [62] Takahashi S, Deacon R S, Oiwa A, Shibata K, Hirakawa K and Tarucha S 2013 Electrically tunable three-dimensional g-factor anisotropy in single In As self-assembled quantum dots *Phys. Rev. B* **87** 161302
- [63] Schwan A, Meiners B M, Greilich A, Yakovlev D R, Bayer M, Maia A D B, Quivy A A and Henriques A B 2011 Anisotropy of electron and hole g-factors in (In,Ga)As quantum dots *Appl. Phys. Lett.* **99** 221914